Supporting information for

Broadband Emission Originated from the Stereochemical Expression of $6s^2$ Lone Pairs in Two-Dimensional Lead Bromide Perovskites

*Xiaofan Jiang[1,2], Yu Tao[1], Jiazhen Gu[1], Leyang Jin[1], Chen Li[1], Wenkai Zhang[2] *, and Yongping Fu[1] **

[1] Beijing National Laboratory for Molecular Science, State Key Laboratory of Rare Earth Materials Chemistry and Applications, College of Chemistry and Molecular Engineering, Peking University, Beijing 100871, China

[2] Department of Physics and Applied Optics Beijing Area Major Laboratory, Center for Advanced Quantum Studies, Beijing Normal University, Beijing 100875, China

* Corresponding author: Email: wkzhang@bnu.edu.cn, yfu@pku.edu.cn

Experimental section

Starting Materials. $PbBr_2$ (99.0%, Aladdin), HBr (48 wt.% in H_2O, Energy Chemical), 4-chlorophenylammonium (99%, Adamas-beta), benzylammonium (99%, Adamas-beta), 4-aminotetrahydropyran (98% *Bide Pharmatech Co., Ltd*).

Synthesis of $(PMA)_2PbBr_4$ and $(ATHP)_2PbBr_4$. Single-crystal $(PMA)_2PbBr_4$ and $(ATHP)_2PbBr_4$ were synthesized by the widely used cooling-induced crystallization method. Specially, 1.0 mmol $PbBr_2$ and 2.0 mmol benzylammonium or 2.0 mmol 4-aminotetrahydropyran were added into a 15 mL reaction vial containing 2 mL HBr aqueous solution. The reaction vial was then placed in a 100°C water bath to dissolve the solids until a clear solution was obtained. By turning off the heating of the water bath, the solution was naturally cooled down to room temperature, and colorless flake-like crystals precipitated.

Synthesis of $(4ClPA)_2PbBr_4$. Single-crystal $(4ClPA)_2PbBr_4$ was synthesized by solvent volatilization method. Specially, 1.0 mmol $PbBr_2$ and 2.0 mmol 4-chlorophenylammonium were added into a 15 mL reaction vial containing 8 mL HBr

aqueous solution. The reaction vial was then placed on a hot plate at 100°C to dissolve the solids until a clear solution was obtained. Subsequently, the temperature of the hot plate was lowered to 60 °C, and the solution was left on the hot plate to slowly evaporate the solvent. Colorless rectangular crystals precipitated within three days.

Single-crystal X-ray Crystallography. The single-crystal X-ray diffraction data were collected on a Rigaku XtalLAB Synergy diffractometer with Cu-Kα radiation (λ = 1.54184 Å). Olex2-1.5 software was used to solve and refine the crystal structure of $(4ClPA)_2PbBr_4$. The CCDC reference number is 2264136.

Optical Characterizations. Temperature-dependent photoluminescence emission (PL) and excitation spectra (PLE) of the three bulk single crystals were measured using a NanoLog infrared fluorescence spectrometer. The monitored emission wavelengths on the PLE measurements were 470, 560, and 550 nm for $(PMA)_2PbBr_4$, $(ATHP)_2PbBr_4$, and $(4ClPA)_2PbBr_4$, respectively. The excitation wavelengths on the PL measurements were 300, 330, and 330 nm, respectively. The polarization-resolved low-frequency Raman spectra were performed on a homebuilt microscope setup with a 633 nm He–Ne laser (N-LHP-925, Newport) as the excitation source, as described in our previous work[1]. The scheme of the Raman measurement is shown in Fig. S7. The excitation laser was filtered from undesirable amplified spontaneous emission using a volume Bragg grating (VBG) bandpass filter (Optigrate, linewidth: 5 cm^{-1}), and then was focused onto the sample by a long working distance ×50 objective (NA 0.4, Nikon). The Raman signal was collected with the same objective and focused into a spectrograph (Princeton Instruments, HRS-300S) and detected by a liquid-nitrogen-cooled charge-coupled device camera (Princeton Instruments, PyLoN-400BRX). To minimize the Rayleigh scattered light, the collected signal was sent through the VBG reflecting filter and passed through three VBG notch filters (Optigrate, OD > 3) before being dispersed in the spectrograph.

Density functional theory (DFT) calculations. We calculated the electronic band structures of $(PMA)_2PbBr_4$, $(ATHP)_2PbBr_4$, and $(4ClPA)_2PbBr_4$ using the Vienna Ab initio Simulation Package (VASP) [2]. The Kohn-Sham density functional theory (KS-DFT) was implemented using a planewave basis set and the projector augmented wave

(PAW) formalism[3] with a cutoff energy of 400 eV. Exchange and correlation were treated with the Perdew−Burke−Ernzerhof (PBE) [4] functional. The VASPKIT package [5] and VESTA program[6] were used in the pre- and post-processing of our computations. To investigate the relations between the localized Pb $6s^2$ electron pair and *sp* hybridization, we further calculated the electron localization function (ELF), projected density of states (PDOS), and integrated projected density of states (IPDOS) of the three structures. To obtain a quantitative description of the strength of *sp* hybridization, we calculated the percentage of 6*p* component in the first peak of DOS below Fermi level, defined as

$$Percentage\ of\ 6p\ component\ = \frac{IPDOS_p}{IPDOS_s + IPDOS_p},$$

where the IPDOS are integrated from -0.1 eV to 0 eV for $(PMA)_2PbBr_4$ and $(ATHP)_2PbBr_4$, and from -0.2 eV to 0 eV for $(4ClPA)_2PbBr_4$, respectively.

The fits of unpolarized low-frequency Raman spectra. The Raman spectrum was deconvolved to a product of the Bose-Einstein distribution and a sum of a Debye relaxational term and multiple Lorentz oscillator terms, which is expressed as[6]:

$$I(\nu,\nu_i,\Gamma_i) = \left(\frac{1}{\exp\left(\frac{h\nu}{k_B T}\right) - 1} + 1\right)\left[\frac{c_0 \nu \Gamma_0}{\nu^2 + \Gamma_0^2} + \sum_{i=1}^{n} c_i \frac{\nu \nu_i \Gamma_i^2}{\nu^2 \Gamma_i^2 + \left(\nu^2 - \nu_i^2\right)^2}\right] \#$$

where h is the Planck constant, k_B is the Boltzmann constant, $T = 298\,K$ is the temperature, ν is the spectral shift, ν_is are the resonance energies of the Stokes Raman modes, Γ_0 and Γ_i are the damping coefficients of the Debye component (the first term in the bracket) and the Lorentz components (the second term in the bracket), c_0 and c_is are the fitting parameters for the intensities of the Debye and Lorentz components, respectively. The fitting results of both Debye and Lorentz components and the fitted peak positions (ν_i) and widths (Γ_i) are summarized in Table S4.

Supporting figures

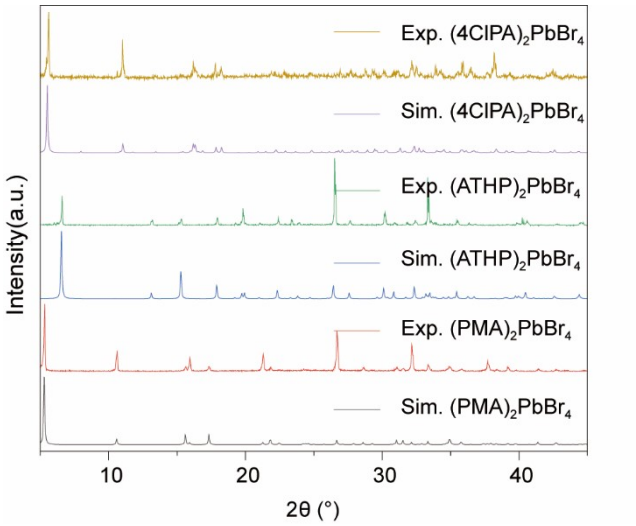

Fig. S1 Powder X-ray diffraction (PXRD) patterns of $(PMA)_2PbBr_4$, $(ATHP)_2PbBr_4$, and $(4ClPA)_2PbBr_4$.

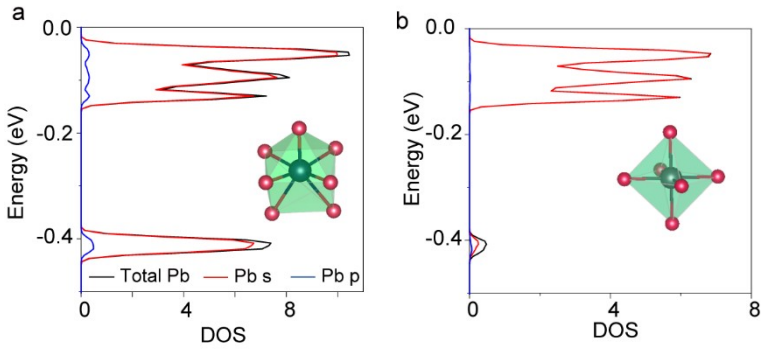

Fig. S2 Orbital projected density of states for Pb s and Pb p contributions in the (a) capped octahedra and (b) regular octahedra of $(4ClPA)_2PbBr_4$.

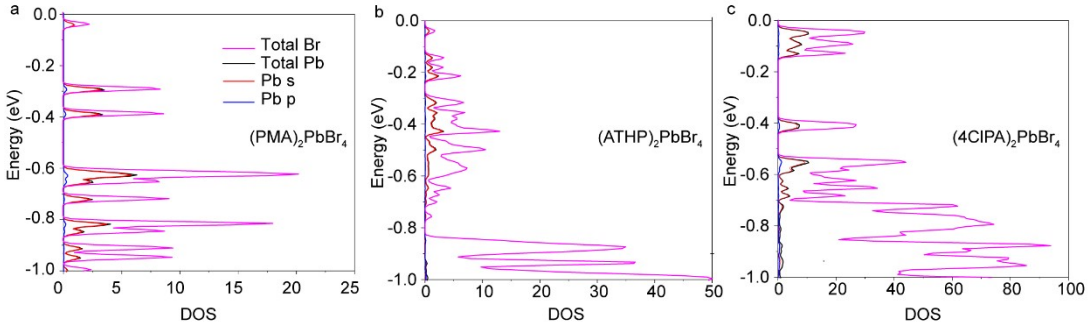

Fig. S3 Orbital projected density of states for Pb and Br contributions in the (a) $(PMA)_2PbBr_4$, (b) $(ATHP)_2PbBr_4$, and (c) $(4ClPA)_2PbBr_4$

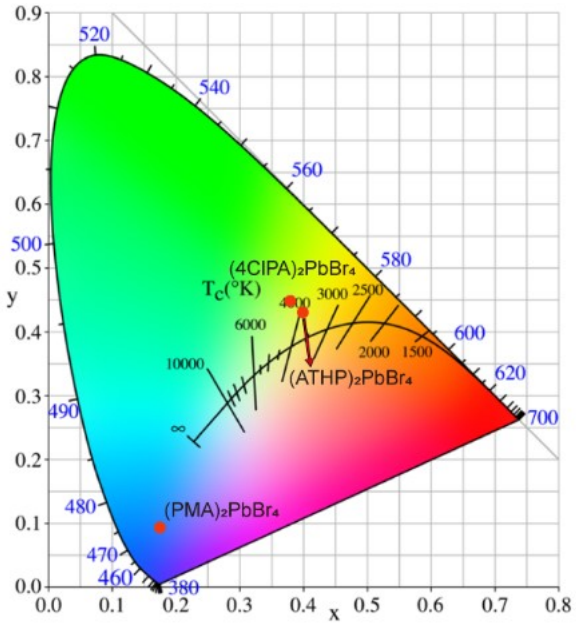

Fig. S4 CIE color coordinates of $(PMA)_2PbBr_4$, $(ATHP)_2PbBr_4$, and $(4ClPA)_2PbBr_4$.

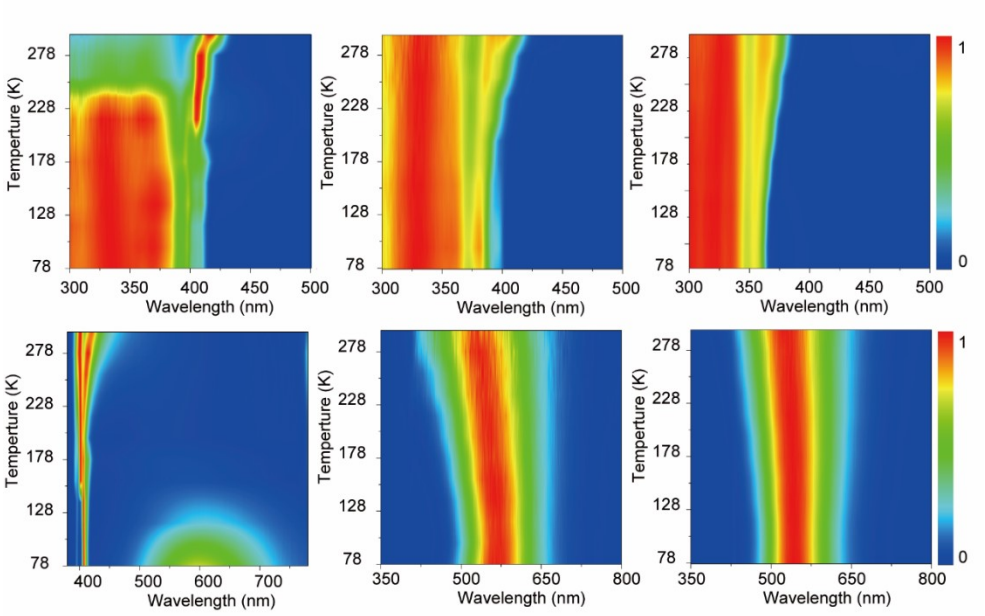

Fig. S5 Temperature-dependent PLE spectra of (a) $(PMA)_2PbBr_4$, (b) $(ATHP)_2PbBr_4$, and (c) $(4ClPA)_2PbBr_4$. The monitored emission wavelengths on the PLE measurements were 470, 560, and 550 nm, respectively. Temperature-dependent of PL spectra of (d) $(PMA)_2PbBr_4$, (e) $(ATHP)_2PbBr_4$, and (f) $(4ClPA)_2PbBr_4$.

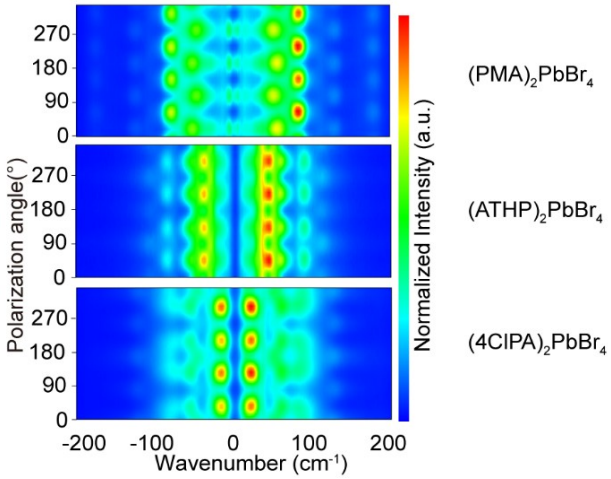

Fig. S6 Polarization-resolved low-frequency Raman spectra of $(PMA)_2PbBr_4$, $(ATHP)_2PbBr_4$, and $(4ClPA)_2PbBr_4$. The dominant Raman peak shifts to lower energy in the sequence of $(PMA)_2PbBr_4$, $(ATHP)_2PbBr_4$, and $(4ClPA)_2PbBr_4$. The polarization of the analyzer is set to be perpendicular to the incident laser polarization.

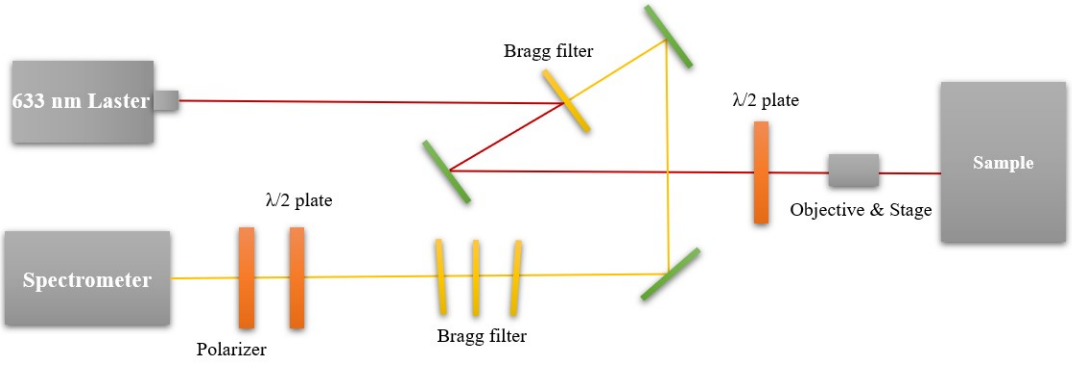

Fig. S7 Scheme of the polarization-resolved Raman measurement.

Supporting Tables

Table S1. Crystal Structure Refinement of $(4ClPA)_2PbBr_4$

Structure	$(4ClPA)_2PbBr_4$
Empirical formula	$C_{12}N_2H_{14}Br_4Cl_2Pb$
Crystal system	Monoclinic
Space group	$P2_1/c$
Unit cell dimensions	a = 16.6366(7) Å, α = 90°
	b = 8.0081(4) Å, β = 105.410(4)°
	c = 23.0142(10) Å, γ = 90°
Volume	2955.9(2) Å^3
Z	6
Index ranges	-16<=h<=19,
	-7<=k<=9,
	-25<=l<=27
Independent reflections	14358 [R_{int} = 0.0715]
Completeness to θ = 29.41°	99.8 %
Data / restraints / parameters	5187 / 79 / 290
Goodness-of-fit	1.054
R_1[a], wR_2[b] [$I>2\sigma(I)$]	0.0565,0.1366
R_1, wR_2 [all data]	0.0738, 0.1510
Largest diff. peak and hole	6.709 and -4.728 e·Å^{-3}

[a] $R = \Sigma||F_o|-|F_c|| / \Sigma|F_o|$.

[b] $wR = \{\Sigma[w(|F_o|^2 - |F_c|^2)^2] / \Sigma[w(|F_o|^2)^2]\}^{1/2}$.

$w=1/[\sigma^2(F_o^2)+(0.0833P)^2+3.5012P]$ where $P=(F_o^2+2F_c^2)/3$.

Table S2. Comparison of the structural and optical properties in $(4ClPA)_2PbBr_4$ and $(4BrPA)_2PbBr_4$

Structure/comparison	$(4ClPA)_2PbBr_4$		$(4BrPA)_2PbBr_4$	
	Capped octahedra	Octahedra	Capped octahedra	Octahedra
Average Pb-Br bond length (Å)	3.106	2.967	3.109	2.967
Average quadratic elongation (<λ>)	-	1.0015	-	1.0005
Average bond angle variance (σ_θ^2, deg^2)	-	0	-	0
Interlayer distance (Å)	10.043		10.327	
PL emission peak (eV)	2.26		2.21	
Excitonic peak (eV)	3.39		3.42	

Table S3. Comparison of the structural and optical in $(ATHP)_2PbBr_4$, $(4\text{-}AMP)_2PbBr_4$ and $(CHA)_2PbBr_4$

Structure/comparison	$(ATHP)_2PbBr_4$	$(4\text{-}AMP)_2PbBr_4$[8]	$(CHA)_2PbBr_4$[9]
Average Pb−Br−Pb angle (out-of-plane) (deg)*	180	180	180
Average Pb−Br−Pb angle (in-plane) (deg)	150	153.24	152.09
FWHM (nm)	106	~107	~153
PL emission peak (eV)	2.16	2.38	2.05

* All the three structures exhibit no out-of-plane distortion, but they exhibit broadband emission.

Table S4. Fitting parameters c_0, c_is and peak widths Γ_0, Γ_is of the fitted Raman spectra of $(PMA)_2PbBr_4$, $(ATHP)_2PbBr_4$ and $(4ClPA)_2PbBr_4$.

LA cation	Debye component		Lorentz component		
	c_0	Γ_0 (cm^{-1})	ν_i (cm^{-1})	c_i	Γ_i (cm^{-1})
PMA	455	24.6	56	3656	28.1
			81	4179	19.0
			127	1088	19.6
			177	1179	33.6
ATHP	646	109.8	35	1099	12.2
			50	2583	26.4
			87.8	998	12.3
			110.0	915	44.6
PMA	1237	79.5	20	857	12.6
			27	976	17.0
			57	2036	24.4
			83	2995	33.6
			125	1078	30.0

References

1 X. Huang, X. Li, Y. Tao, S. Guo, J. Gu, H. Hong, Y. Yao, Y. Guan, Y. Gao, C. Li, X. Lü and Y. Fu, *J. Am. Chem. Soc.*, 2022, **144**, 12247–12260.

2 G. Kresse and J. Furthmüller, *Phys. Rev. B*, 1996, **54**, 11169–11186.

3 P. E. Blöchl, *Phys. Rev. B*, 1994, **50**, 17953–17979.

4 J. P. Perdew, K. Burke and M. Ernzerhof, *Phys. Rev. Lett.*, 1996, **77**, 3865–3868.

5 V. Wang, N. Xu, J.-C. Liu, G. Tang and W.-T. Geng, *Comput. Phys. Commun.*,

2021, **267**, 108033.

6 K. Momma and F. Izumi, *J. Appl. Crystallogr.*, 2011, **44**, 1272–1276.

7 L. Gao, L. Yadgarov, R. Sharma, R. Korobko, K. M. McCall, D. H. Fabini, C. C. Stoumpos, M. G. Kanatzidis, A. M. Rappe and O. Yaffe, *Mater. Adv.*, 2021, **2**, 4610–4616.

8 L. Mao, P. Guo, M. Kepenekian, I. Hadar, C. Katan, J. Even, R. D. Schaller, C. C. Stoumpos and M. G. Kanatzidis, *J. Am. Chem. Soc.*, 2018, **140**, 13078–13088.

9 A. Yangui, D. Garrot, J. S. Lauret, A. Lusson, G. Bouchez, E. Deleporte, S. Pillet, E. E. Bendeif, M. Castro, S. Triki, Y. Abid and K. Boukheddaden, *J. Phys. Chem. C*, 2015, **119**, 23638–23647.